Inorganic Chemistry

Article

pubs.acs.org/IC

Bonding and Charge Transfer in Nitrogen-Donor Uranyl Complexes: Insights from NEXAFS Spectra

C. D. Pemmaraju,*[,†,‡] Roy Copping,[‡,⊗] Shuao Wang,[‡,○] Markus Janousch,[‡,#] Simon. J. Teat,[⊥] Tolek Tyliszcak,[⊥] Andrew Canning,[§,∥] David K. Shuh,[‡] and David Prendergast[†]

[†]The Molecular Foundry, [‡]Chemical Sciences Division, The Glenn T. Seaborg Center, [∥]Computational Research Division, and [⊥]Advanced Light Source, Lawrence Berkeley National Laboratory, Berekeley, California 94720, United States

[§]Department of Chemical Engineering and Materials Science, University of California, Davis, California 95616, United States

[#]Laboratory for Synchrotron Radiation, Paul Scherrer Institute, Villigen, 5232 Switzerland

Supporting Information

ABSTRACT: We investigate the electronic structure of three newly synthesized nitrogen-donor uranyl complexes $[(UO_2)(H_2bbp)Cl_2]$, $[(UO)_2(Hbbp)(Py)Cl]$, and $[(UO_2)(bbp)(Py)_2]$ using a combination of near-edge X-ray absorption fine structure (NEXAFS) spectroscopy experiments and simulations. The complexes studied feature derivatives of the tunable tridentate N-donor ligand 2,6-bis(2-benzimidazyl)pyridine (bbp) and exhibit discrete chemical differences in uranyl coordination. The sensitivity of the N K-edge X-ray absorption spectrum to local bonding and charge transfer is exploited to systematically investigate the evolution of structural as well as electronic properties across the three complexes. A thorough interpretation of the measured experimental spectra is achieved via *ab initio* NEXAFS simulations based on the eXcited electron and Core-Hole (XCH) approach and enables the assignment of spectral features to electronic transitions on specific absorbing sites. We find that ligand−uranyl bonding leads to a signature blue shift in the N K-edge absorption onset, resulting from charge displacement toward the uranyl, while changes in the equatorial coordination shell of the uranyl lead to more subtle modulations in the spectral features. Theoretical simulations show that the flexible local chemistry at the nonbinding imidazole-N sites of the bbp ligand is also reflected in the NEXAFS spectra and highlights potential synthesis strategies to improve selectivity. In particular, we find that interactions of the bbp ligand with solvent molecules can lead to changes in ligand−uranyl binding geometry while also modulating the K-edge absorption. Our results suggest that NEXAFS spectroscopy combined with first-principles interpretation can offer insights into the coordination chemistry of analogous functionalized conjugated ligands.

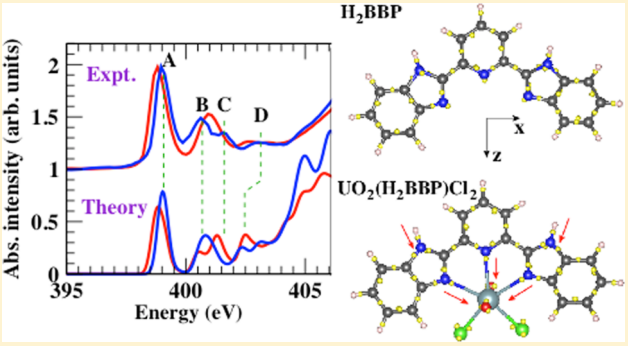

1. INTRODUCTION

Over the last two decades, the richness of uranium coordination chemistry has been actively explored leading to the synthesis and characterization of a large diversity of compounds exhibiting novel structural, physical, and catalytic properties.[1] The uranyl $\{UO_2\}^{2+}$ cation in particular has received a great deal of attention both from experimental and theoretical groups as new aspects of its chemistry continue to be discovered.[2,3] Recent years have witnessed several advances in uranyl(VI) anhydrous chemistry with polarizable donor atoms (such as nitrogen and sulfur) and weakly coordinating ligands being employed[4−7] as opposed to hard donor (i.e., oxygen) systems traditionally studied in aqueous conditions. $\{UO_2\}^{2+}$ exhibits quite versatile chemistry in soft donor systems with multidentate ligands adopting strained coordination geometries about the uranyl to satisfy the equatorial coordination sphere.[4,8] Furthermore, investigations into bonding and covalency in $\{O{=}U{=}O\}^{2+}$ molecular complexes[9−16] have been enhancing the understanding of the structural, electronic, and chemical aspects of this moeity.

In this context, three new N-donor uranyl complexes featuring the tridentate N-donor ligand 2,6-bis(2-benzimidazyl)pyridine (H_2bbp), namely, $[UO_2(H_2bbp)Cl_2]$ (**1**), $[UO_2(Hbbp)(Py)Cl]$ (**2**), and $[UO_2(bbp)(Py)_2]$ (**3**) have recently been synthesized, and their structural characteristics have been determined.[17] H_2bbp is a versatile N-donor ligand, which has previously been studied as a sensitizer for lanthanide luminescence as well as a low-valent actinide sequestering agent.[18−23] It presents one pyridine-like and two imidazole-like N binding sites (see Figure 1) in a largely π-conjugated structure that can readily polarize to accommodate functional group attachment. We refer to the organic framework common to H_2bbp and its deprotonated derivatives

Received: May 15, 2014
Published: October 20, 2014

   dx.doi.org/10.1021/ic501107a | *Inorg. Chem.* 2014, 53, 11415−11425

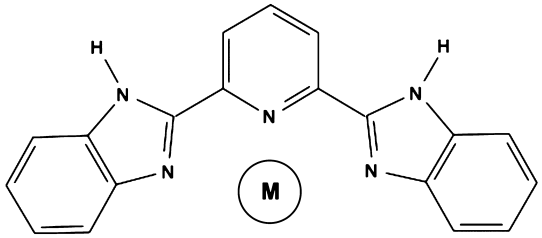

Figure 1. Schematic of the tridentate N donor ligand 2,6-bis(2-benzimidazyl)pyridine (bbp). M indicates the metal binding site.

as bbp, bbp^-, or bbp^{2-} explicitly indicating that the charge state of the ligand is pertinent. The chemistry of H_2bbp is sufficiently flexible to produce complexes with different chemical groups bonded to the uranyl moeity in the equatorial coordination plane perpendicular to the uranyl axis. In complexes **1**−**3**, the bbp ligand character changes from neutral (bbp) to harder mono- (bbp^-) and di- (bbp^{2-}) deprotonated species, and the hard-donor Cl^- groups in **1** to dative and more basic pyridine groups in **3**. Exploring the evolution of the structural and electronic properties of the uranyl−bbp system as a function of changing ligand character is a worthwhile approach to improve the understanding of N-donor uranyl coordination chemistry.

In-depth experimental characterization of the electronic structure of actinide complexes is facilitated by element-specific and bulk-sensitive X-ray absorption spectroscopy (XAS) techniques such as Near Edge X-ray Absorption Fine Structure (NEXAFS).[24−26] In XAS, X-ray photons are absorbed by core electrons of an atom within a molecule or crystal, which promotes the electrons to higher-lying unoccupied orbitals forming short-lived excited states. The onset of excitations from the core−shells of an atom gives rise to an element-specific absorption edge such as the K-edge for 1s excitations. NEXAFS refers to the fine details in the absorption spectrum in the vicinity of such an edge and effectively probes the low-energy excited states of a system yielding valuable information about local structure, symmetry, and oxidation state as well as bonding characteristics. The Scanning Transmission X-ray Microscope (STXM), which utilizes soft X-ray synchrotron radiation (less than ∼5000 eV) to probe light element K (1s) and actinide $N_{IV/V}$ ($4d_{3/2,5/2}$) edges by NEXAFS, is particularly useful for studying actinide-based systems in which air-sensitivity and small sample size issues must be considered.[27] The interpretation of measured NEXAFS spectra is, however, not straightforward, and theoretical methods are often indispensible to explain the various spectral features. A number of theoretical methods have been developed over the past decade to reproduce and explain experimental core-level spectra, and in particular, the availability of modern first-principles techniques[26,28−31] has enabled the quantitative interpretation of NEXAFS data.

Light element K-edges in uranyl complexes are sensitive to the bonding environment and can be probed by XAS to gain insight into uranyl−ligand covalent interactions.[11,14,32,33] Furthermore, the high resolution offered by soft X-ray sources makes the study of light element K-edges more useful compared to higher energy $N_{IV/V}$ edges of the actinide ions themselves, which suffer from intrinsic broadening. In particular, investigating the electronic structre of N-donor uranyl complexes using N K-edge NEXAFS is very promising but has not been undertaken thus far. The polarizable character of N in bbp provides a larger variability in the spectra compared to hard donors such as oxygen. Within complexes such as **1**−**3**, modulation of the electronic structure on the different N sites spanning the bbp framework, as a result of tuning the ligand chemistry around the uranyl, can in principle be effectively probed via K-edge core-level spectroscopy. Toward this end, we combine experimental X-ray absorption measurements and first-principles theoretical simulations of the N K-edge NEXAFS spectra of complexes **1**−**3**. This enables a thorough interpretation of the spectral features in terms of the underlying electronic structure and uranyl−bbp bonding characteristics. The U $N_{IV/V}$ spectra from the complexes being investigated have been published previously.[17]

2. EXPERIMENTAL DETAILS

The key to realizing complexes **1**−**3** is the synthesis of suitable precursors with distinct chemical differences that can complex with $\{UO_2\}^{2+}$. To this end, the free base derivative H_2bbp and corresponding deprotonated mono- and disodium substituted salts were synthesized and subsequently reacted with $UO_2Cl_2(THF)_3$ to yield complexes **1**−**3**. Complete details of the synthesis are reported elsewhere.[17] STXM data were obtained at the Advanced Light Source (ALS), Molecular-Environmental Sciences (MES) beamline 11.0.2 at Lawrence Berkeley National Laboratory. Beamline 11.0.2 utilizes a STXM for NEXAFS at the light element thresholds and at the actinide $N_{IV/V}$ ($4d_{3/2,5/2}$) core level edges. The MES STXM can image and collect NEXAFS from particles with spatial resolution better than 25 nm in the range from 110 to 2100 eV. The STXM is downstream of an elliptical polarization undulator (EPU) and a variable angle-included plane grating monochromator that is used routinely to collect K-edge NEXAFS data from low Z atoms. STXM measurements were collected from minute quantities of powdered solids of the uranyl complexes sealed between two Si_3N_4 windows in a STXM holder, with care being taken to avoid atmospheric exposure.[17,27] The N spectra were taken with horizontal EPU polarization and calibrated to the absorption line of the 1s → π^* transition (401.1 eV) in N_2. No polarization dependence was found in the measured spectra. All reported spectra are normalized to the incoming flux with backgrounds subtracted and subsequently smoothed using a three- or five-point method.

3. COMPUTATIONAL METHODOLOGY

A quantitative theoretical description of the spectroscopic properties of bbp−uranyl complexes poses several challenges because of the large system sizes that need to be considerd and the highly inhomogeneous nature of the electron density in these complexes. While accurate multiconfigurational wave function methods have been employed to study small actinide systems,[34,35] large molecular crystals such as the ones that are the subject of this study are only accessible within a density functional theory[36,37] (DFT)-based approach. In this context, the localized nature of 5f electrons and the possibility of strong electron correlation effects needs to be taken into account even though the 5f shell of U(VI) in the uranyl cation is nominally empty. In contrast, the delocalized virtual molecular orbitals, which we observe to span the entire bbp unit in the ground state (GS) are significantly altered in the presence of a core hole, and so, a description of the NEXAFS spectrum in terms of excitations to virtual GS orbitals is not useful. Furthermore, relative core excitation energies between chemically different binding N sites on the ligands need to be modeled accurately to capture correctly the contribution of each to the measured composite spectrum. With this in mind, we carry out our theoretical studies using the so-called eXcited electron and Core-Hole (XCH) approach[31], which is quickly becoming a robust methodology for NEXAFS simulations based on constrained-occupancy DFT. We calculate the X-ray absorption cross section to first order using Fermi's golden rule

$$\sigma(\omega) = 4\pi^2\alpha_0\hbar\omega \sum_f |M_{i\to f}|^2 \delta(E_f - E_i - \hbar\omega)$$

dx.doi.org/10.1021/ic501107a | Inorg. Chem. 2014, 53, 11415−11425

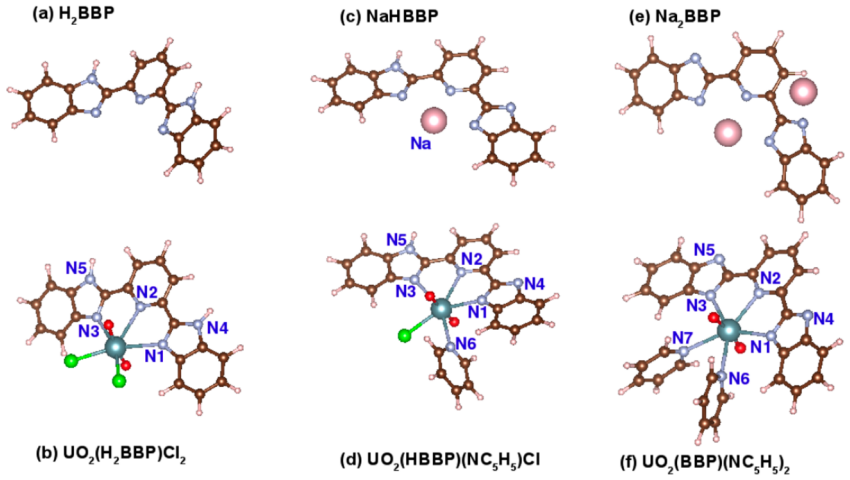

Figure 2. Ball-and-stick representations of the structures of uranyl complexes and their corresponding precursors. Nitrogen sites in the complexes are labeled for clarity. The color code is as follows: O (red), Cl (green), C (brown), U (blue, large), Na (pink), H (white).

The transition amplitudes between initial and final states $M_{i\to f}$ are evaluated using the dipole approximation within a single-particle picture

$$M_{i\to f} = <\Psi_f|\vec{\varepsilon}\cdot\vec{R}|\Psi_i> \approx S < \psi_f|\vec{\varepsilon}\cdot\vec{r}|\psi_i>$$

where $\vec{\varepsilon}$ is the polarization direction of the photon electric field and $\vec{R}$, $\vec{r}$ are the many and single-particle position operators, respectively. The single-particle approximations of the many-electron matrix elements are accurate up to a factor $S \leq 1$ approximated as constant for all transitions.[38]

The framework for our calculations is set by pseudopotential-based Kohn–Sham DFT[36,37] employing planewave basis sets and periodic boundary conditions. For X-ray core-hole excitations at light element K-edges the initial state $|\psi_i\rangle$ is fixed to the 1s atomic eigenstate of the respective element. The XCH approach[31] is employed to approximate the electronic final state $|\psi_f\rangle$ within the Fermi golden rule expression as follows: The core-level excited state of the molecule is approximated by replacing the pseudopotential of the core-excited atom with one that explicitly includes a core excitation. We also include the important screening presence of the excited electron. We then generate a self-consistent set of Kohn–Sham valence states in the presence of both the core hole and the excited electron. The resulting constrained DFT solution approximates the lowest energy state of the system including a core-excited state of the perturbed atom. The higher excited states are further approximated by using the unoccupied Kohn–Sham spectrum of this XCH self-consistent field. The energy scale of the spectra in XCH calculations needs to be shifted in a systematic way to be compared to experiment.[39,40] For a given chemical system X in which an atom of element A is excited, the energy scale is shifted as follows

$$E \to E - \varepsilon_{N+1}^{XCH} + \Delta E_A^X + \Delta_{expt}[A]$$

where ε_{N+1}^{XCH} is the value of $(N+1)$ or lowest unoccupied molecular orbital (LUMO) eigenvalue of the core-excited system. Note that in a spin-upolarized molecular system, this state is half-occupied. In a condensed-phase calculation, ε_{N+1}^{XCH} is given appropriately by an estimate of the partially occupied conduction band minimum. ΔE_A^X is the relative excitation energy of X with respect to an isolated atom of A given by total energy differences as

$$\Delta E_A^X = [E^{XCH}(X) - E^{GS}(X)] - [E^{XCH}(A) - E^{GS}(A)]$$

with E^{XCH} and E^{GS} denoting the total energies in the core-excited and groundstate configurations, respectively, for a given system X or A. The final shift with respect to experiment $\Delta_{expt}[A]$ is calculated once for a given reference system and remains the same for all systems in which an atom of element A is excited.

The XCH method can be combined seamlessly with DFT+U[41,42] to approximate strong correlation effects. In particular, we employ the self-consistent DFT+U[42,43] approach wherein the Hubbard U parameter is determined self-consistently from linear response:

$$U = \chi_0^{-1} - \chi^{-1}$$

where

$$\chi_{IJ} = \frac{dn_I}{d\alpha_J}$$

is the response coefficient obtained from applying an arbitrary shift α_J to the potential on the atomic site J that results in a change of the occupation n_I on site I. χ_0 is the corresponding nonselfconsistent analog.

Ground-state DFT calculations in this work were carried out using the VASP[44] and Quantum-Espresso[45] packages. The Perdew, Burke, and Ernzerhof (PBE)[46] form of the generalized gradient approximation to the exchange correlation functional was used throughout. All structural optimization runs were performed at the PBE level, using the VASP package, which employs projector augmented wave (PAW) pseudopotentials[47] in conjunction with a planewave basis set. A planewave cutoff of 300 eV and pseudopotentials with the following valence electronic configurations were employed: U($6s^26p^66d^15f^37s^2$), O($2s^22p^4$), C($2s^22p^2$), N($2s^22p^3$), Cl($3s^23p^5$), H($1s^1$). Structures were optimized until all the forces were less than 0.04 eV/Å. Within Quantum Espresso, ultrasoft pseudopotentials with the same valence electron configuration as before and a planewave cutoff of 40 Ry were used. NEXAFS simulations were performed on primitive cells of molecular crystals of complexes **1**–**3** containing two to four molecular units. Because of the large unit cell sizes of the molecular crystals, for all the systems considered, we approximated Brillouin zone integration by sampling only the zone center (i.e., the Γ point), while necessarily numerically converging the integration for NEXAFS spectra using Shirley interpolation.[48] A uniform numerical broadening of 0.2 eV was applied to the theoretical spectra. To determine the Δ_{expt} parameter within the XCH approach for N K edge spectra, an isolated N_2 molecule was used as a reference system, which yielded $\Delta_{expt}[N_{1s}]$ = 396.5 eV for the core-excited pseudopotentials employed in this study. All other calculated N K-edge spectra were rigidly shifted by this amount. Molecular orbital plots were obtained using the VESTA[49] visualization program.

4. RESULTS

4.1. Structural Properties. Figure 2 shows structural models of the uranyl complexes and the corresponding precursors. All systems contain at least five N sites (N1–N5)

dx.doi.org/10.1021/ic501107a | Inorg. Chem. 2014, 53, 11415–11425

from the bbp ligand framework and additional N sites from pyridine (Py) ligands where present. Three different types of N sites can be identified in H_2bbp. Atoms N1 and N3 on the benzimidazole segments are only 2-fold coordinated and host lone pairs of electrons. Atom N2 on the central pyridine also hosts a lone pair of electrons and is therefore chemically similar to N1 and N3. These three N atoms constitute the primary tridentate binding site for incoming metal atoms. In contrast, the outer N4 and N5 nitrogens are protonated and are therefore less reactive. In complex **1**, a uranyl group is bonded to sites N1−N3 of the bbp ligand. Additionally, two hard-donor Cl^- ions ligating the uranyl complete the pentagonal coordination in the equatorial plane of the linear $\{O{=}U{=}O\}^{2+}$. Synthesis of the mono- and disodium salts of H_2bbp, namely, NaHbbp and Na_2bbp, involves successive deprotonation of the outer imidazole nitrogens N4 and N5 (see Figure 2). Additionally, complexes **2** and **3** differ from **1** in having Cl^- ions successively replaced by Py ligands.

Structural parameters of molecular crystals of **1**−**3** were determined from X-ray diffraction measurements and analyzed with the help of ground-state DFT calculations.[17] Structural properties exhibit a systematic trend across the three complexes driven by the gradual relaxation of steric hindrance and elevated charge on the bbp ligand as the Cl^- ions are successively replaced by pyridine groups going from **1** to **3**. Steric hindrance imposed by the large ionic radius of the bonded chlorides forces the H_2bbp ligand in **1** to adopt a nonplanar bonding geometry about the uranyl. DFT total energy calculations have confirmed[17] that this equatorial nonplanarity is intrinsic to the molecule and is not a result of crystal formation and associated neighbor interactions. Almost perfect equatorial planarity is restored in complex **3** where both of the chloride ions have been replaced by pyridines with the ligand Py plane perpendicular to the equatorial plane of UO_2. Progressively increasing charge on the bbp ligand and relaxation of the steric constraints also results in a tighter bbp geometry around the uranyl with average U to bbp N distances contracting from 2.58 Å in **1** to 2.51 Å in **3**. In turn, increasing deviation of the uranyl group from linearity is also observed, suggesting a slight weakening of the U═O bonds from **1** to **3**.

During synthesis, complexes **1**−**3** are precipitated out of pyridine or pyridine/benzene solution as molecular crystals.[17] Interactions between molecular units in these crystals are weak. However, in crystallized samples of complexes **1** and **2**, X-ray diffraction (XRD) structure determination indicated additional solvent pyridine molecules were incorporated into the crystalline framework facilitated by hydrogen bonding to bbp. These solvent molecules are also found to affect the internal structure of the complexes especially in the case of **2**. Calculated U−N bond-lengths in complex **2**, from structural models with and without solvent molecules incorporated, are compared to XRD experimental bond-lengths in Table 1.

Table 1. Comparison with Experiment of Calculated U−N Bond Lengths in Complex 2 with and without the Inclusion of Additional Pyridine Solvent Molecules

		theory (Å)	
bond	expt (Å)	with solvent	no solvent
U−N1	2.533(4)	2.542	2.526
U−N2	2.573(4)	2.58	2.600
U−N3	2.593(4)	2.608	2.620

Evidently, in the absence of H bonding between solvent pyridines and the outer N4/N5 sites, the U−N bond lengths on the inner N1−N3 sites exhibit a wider spread. Furthermore, total energy calculations show that the binding energy of the uranyl to the bbp ligand in isolation is enhanced by ∼141 meV in the presence of coordinating solvent Py molecules relative to the case without solvent. This suggests the possibility of functionalizing bbp at the outer imidazole N sites[20,22] to tune the binding and selectivity of the ligand. Interestingly, this also affects the spectroscopic features in these complexes as we will discuss in the next section.

4.2. Ground-State Electronic Properties. We first study the ground-state electronic structure of complexes **1**−**3** within a DFT+U[41,42] framework. The process of determining the Hubbard-U parameter self-consistently for each of the three complexes provides valuable insights into evolution of the local electronic structure around the uranyl. The 5f shell of uranium in the uranyl cation $\{UO_2\}^{2+}$ is formally empty because of its U(VI) oxidation state. Nevertheless hybridization with the 2p shell of oxygen lends the occupied density of states (DOS) some 5f character a few electronvolts below the valence band maximum (see Figure 3). Table 2 shows the on-site U-5f electron occupancies and the self-consistent value of the Hubbard-U parameter for **1**−**3**. The on-site orbital occupancies are calculated by projecting the valence wave functions onto atomic orbital projectors centered on the U site. We see that the 5f occupancy decreases, and in turn the on-site Hubbard-U increases going from complex **1**−**3**. The 5f population on the U site is dictated predominantly by the extent of hybridization with uranyl O 2p and ligand Cl 3p orbitals.

As interactions with Cl^- ions that are principally ionic but with some small degree of covalency[13,14] are successively replaced by dative interactions with N-donor atoms of Py in **2** and **3**, the effective U 5f population is reduced. Furthermore, it is known that strongly donating ligands in the equatorial plane can affect the strength of the U═O bond of uranyl.[3] Thus, we effectively see a slight weakening of U 5f hybridization from **1**−**3** and the 5f states becoming more atomic-like, which is reflected in the increasing Hubbard-U value. Furthermore, as one would expect for less than half occupancy, including the Hubbard-U correction also reduces the on-site 5f population relative to the U = 0 case.

The DOS for complexes **1**−**3**, obtained from both PBE and PBE+U calculations, is shown in Figure 3. As a common feature we see that the average energy position of the occupied U 5f DOS is shifted lower going from **1**−**3**. The main diffence between PBE and PBE+U DOS is in the position of the empty 5f manifold of states. The PBE functional is expected to underestimate the energy position of the virtual 5f states owing to the self-interaction error.[50] As a result the lowest-lying virtual orbitals in PBE are 5f in character and are separated in energy by 0.4−1.2 eV from the ligand-derived π^* states. PBE+U largely corrects for this under-estimation with the result that the empty 5f DOS is raised to higher energies and lies roughly at the same energy as the low-lying π^* states on the ligands.

4.3. Core-Excited Electronic Properties. In the presence of a 1s core-hole, the local potential around a core-excited N site would be substantially deeper. Within a constrained DFT calculation including the effect of a core-hole, this change is reflected as a significant alteration of the DOS relative to the ground state. Accordingly, the π^* states centered on the excited atom now occur at a lower energy than empty U 5f states. The DOS for the lowest-energy constrained excited states of

dx.doi.org/10.1021/ic501107a | Inorg. Chem. 2014, 53, 11415−11425

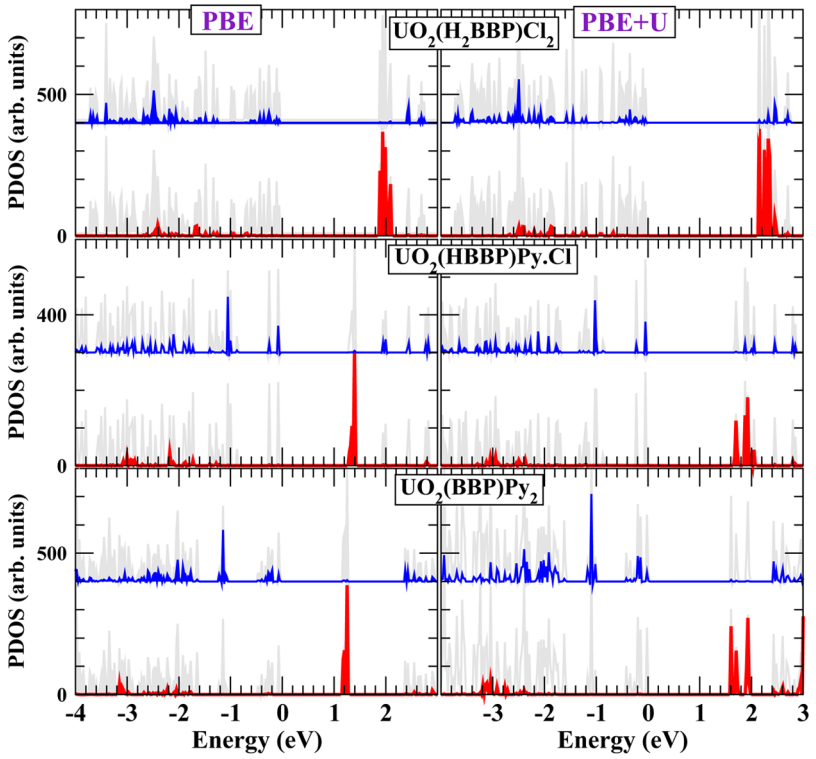

Figure 3. Ground-state projected density of states (PDOS) from PBE (left) and PBE+*U* (right) calculations for the three uranyl complexes. In each panel, the upper blue shaded region is the PDOS for N 2p states, and the lower red shaded area is that of U 5f. The gray shaded background in each case is the total DOS of the system. The valence band maximum is aligned to 0 eV.

Table 2. Projected on-Site 5f Electron Occupancy n_f on a Single Uranium Site within Each Complex and the Calculated Value of the Self-Consistent Hubbard-*U* Parameter U_{scf} Are Shown

complex	$n_f(0)^a$	$n_f(U)^b$	U (eV)
$UO_2(H_2bbp)Cl_2$	1.65	1.60	1.44
$UO_2(Hbbp)Py{\cdot}Cl$	1.62	1.57	1.86
$UO_2(bbp)Py_2$	1.59	1.51	2.48

$^a n_f(0)$ is the occupancy at $U = 0$. $^b n_f(U)$ denotes the occupancy at $U = U_{scf}$.

complexes **1**−**3** for a 1s excitation on site N1 is shown in Figure 4. We see that the conduction band minimum, now occupied by the core-excited electron, is predominantly of N 2p and C 2p character with π^* symmetry (see Figure 6).

Experimental and theoretical NEXAFS spectra for molecular crystals of complexes **1**−**3** and their precursors are shown in Figure 5. Four main features, labeled A, B, C, and D, are identified in the experimental spectra, and their energy positions are reported in Table 3. In general, spectral features observed in the uranyl complexes are also present in the corresponding precursors but occur at slightly different energy positions or with different intensities. One common trend that can be identified is that the primary peak A in each of the three complexes is shifted higher in energy by ∼0.2 eV compared to the precursor. This shift is attributed to a deepening of the N 1s core level in the complex relative to the precursor because of charge transfer from bbp toward the uranyl upon complexation. Furthermore, while features A and B are clearly observed in all the complexes, peak C is not apparent in complexes **2** and **3**, and peak D is not observed in complex **3** even though it is observed in the corresponding precursor (peak *D*′).

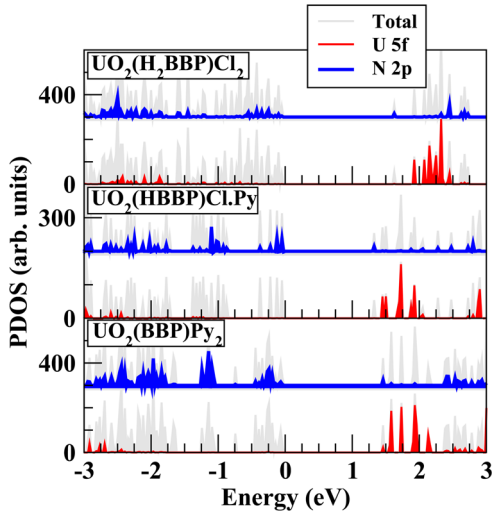

Figure 4. Projected electronic density of states from PBE+*U* for the lowest-energy state including a 1s core-hole on the N1 site of each complex. Note that in this case, the conduction band minimum is partially occupied by the excited core electron. The valence band maximum is aligned at 0 eV for clarity.

We find broadly good agreement between theoretical and experimental spectra especially for energies within a few electronvolts of the absorption onset. Energy positions of higher-lying excitation peaks such as peak D are underestimated by ∼0.5−0.8 eV in the calculations, and in particular, 1s to σ^* excitation energies occurring beyond 405 eV are systematically underestimated by ∼2 eV relative to experiment. This is attributed to the semilocal PBE exchange-correlation functional, which generally underestimates π^*−σ^* splittings, a limitation

dx.doi.org/10.1021/ic501107a | *Inorg. Chem.* 2014, 53, 11415−11425

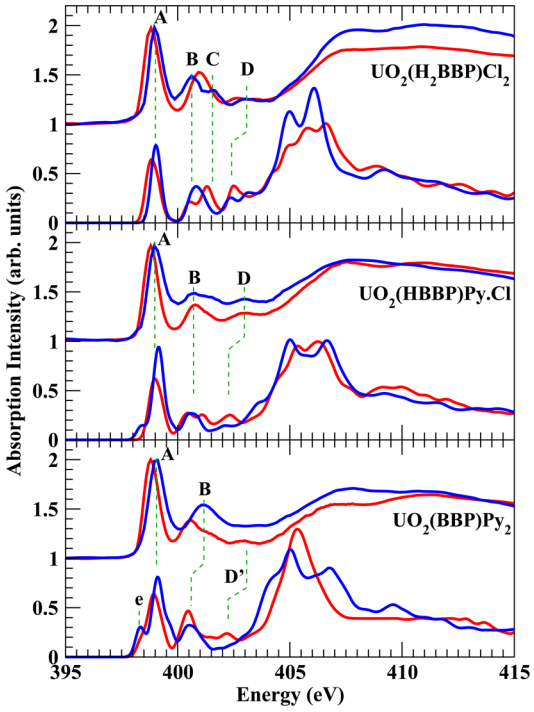

Figure 5. Experimental and simulated N K-edge NEXAFS spectra for uranyl complexes **1**−**3** and their respective precursors. Blue lines depict the spectra for the complexes, while red lines depict those of the precursors. In each panel, the upper spectra are from experiment, with the simulated spectra appearing below them.

that can be rectified by including many-body corrections on top of DFT.[51] In Figure 6 we deconvolute the theoretical spectrum of complex **1** and its precursor H_2bbp into contributions from excitations on different N sites. We see that peak A at ∼399 eV is primarily a 1s → π^* excitation on the central Py site N2. Peak A also has contributions from a 1s → π^* excitation on the imidazole sites N1 and N3. Only the spectrum for an excitation on N1 is shown as that from N3 is almost identical by mirror symmetry. Peaks B (400.7 eV) and C (401.5 eV) are seen to be a combination of two different closely spaced excitations: The second 1s → π^* transition on N1 and the first 1s → π^* excitation on the outer protonated imidazole site N4 (N5 has a similar contribution). The energy spacing between features B and C in complex **1** is slightly underestimated in the calculations with respect to experiment, and so, feature C does not appear as a distinct peak in the theoretical spectrum. Peak D is primarily from the second 1s → π^* excitation on N4/N5 with some contribution also from the third 1s → π^* transition on N1.

Table 3. Major Features Observed within the First Few Electronvolts of the Experimental NEXAFS Spectra of Complexes 1−3 are Reported and Labelled to Be Consistent with Figure 5

label	$UO_2(H_2bbp)Cl_2$[a]	$UO_2(Hbbp)Py{\cdot}Cl$[a]	$UO_2(bbp)Py_2$[a]
A	399.0 (398.8)	399.0 (398.8)	399.0 (398.8)
B	400.7 (401.0)	400.8 (400.8)	401.2 (400.6)
C	401.5		
D	402.7 (403.1)	402.9 (402.9)	−(402.8)

[a]The numbers in parentheses are energies of corresponding features in the precursors.

4.3.1. Spectral Signatures of Charge Density Variation. The blue shift of the absorption onset in the uranyl complex relative to the precursor seen in experiment is also confirmed by theory. This is attributed to deeper N 1s core levels in the complexes because of charge transfer toward the uranyl. Polarization of the electron cloud on the bbp ligand upon complexation with the uranyl can be studied by following the change in the centers of Maximally Localized Wannier functions (MLWFs)[52] in the electronic ground-state. The

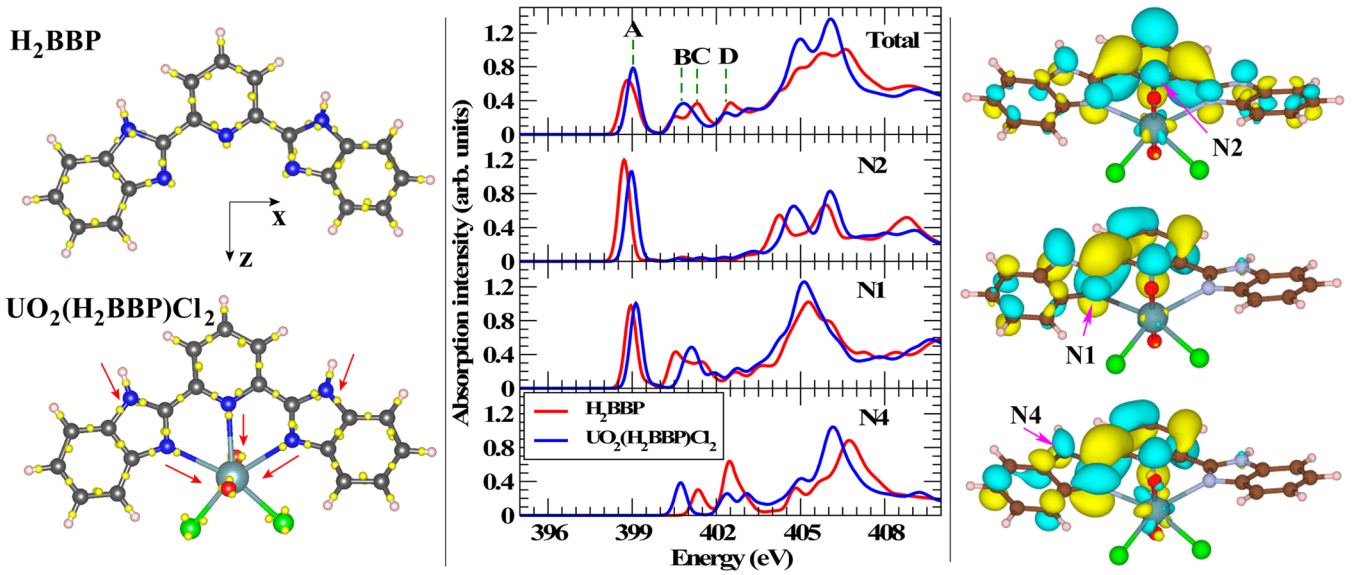

Figure 6. (left) Structural models of H_2bbp and complex **1** indicating the positions of Wannier centers (yellow dots). Red arrows depict schematically the displacement of Wannier centers at N sites on bbp as a result of complexation with uranyl. (middle) Theoretical N K-edge NEXAFS spectra of H_2bbp and complex **1** are decomposed into contributions from excitations on specific N sites. Spectra from the complex are shown in blue, and those from the precursor are shown in red. Features in the total NEXAFS spectrum of the complex (upper) are labeled to be consistent with Figure 5. (right) Electronic wave functions corresponding to the lowest constrained 1s core-hole excited state on specific N sites in complex **1**.

dx.doi.org/10.1021/ic501107a | *Inorg. Chem.* 2014, 53, 11415−11425

centers of MLWFs spanning the occupied subspace provide a heuristic map of the local polarization field, and the displacement of these centers under an external perturbation can be related to the change in polarization.[52] MLWFs reduce to Boys[53] localized fuctions for molecules. In Figure 6, we show structural models of H_2bbp and complex **1** indicating the positions of Wannier centers (yellow dots) corresponding to the occupied manifold. Wannier centers on H_2bbp representing the lone pairs on the N sites N1, N2, and N3 are displaced by ∼0.08 Å toward the uranyl group in complex **1**, indicating the formation of a dative bond. This is represented schematically in Figure 6 by red arrows. Polarization of the electron density on the bbp ligand can also be estimated approximately by considering the bbp as a fragment and treating the ion cores and electrons on this fragment as point charges, with the electrons being located at the Wannier centers. Note that for the precursor H_2bbp, the fragment is the entire molecule. The dipole moment estimated as

$$\mathbf{p} = q_I \mathbf{r}_I - 2e\mathbf{r}_W$$

wherein q_I is the ionic charge, e is the electron charge, $\mathbf{r}_W$ and $\mathbf{r}_I$ are, respectively, the MLWF and ion centers on the bbp alone, increases from −6.94 $\hat{\mathbf{z}}D$ to −8.20 $\hat{\mathbf{z}}D$ going from H_2bbp to **1**, with $\hat{\mathbf{z}}$ pointing toward the uranyl (see Figure 6). It is this charge displacement, which leads to increased binding energy of the N 1s core-levels on bbp, that is the origin of the spectral blue shift.

The full magnitude of the relative core-level shift ΔE_{XPS} between a complex and its precursor can be estimated from a difference in 1s photoionization energies, which can be calculated via ΔSCF DFT calculations as a total energy difference between netural and core-ionized species. Calculated values of the N 1s core-level shifts between complex **1** and H_2bbp, for different N sites, are shown in Table 4 and compared to the corresponding shifts in the NEXAFS onset. Sites N1 and N2/N3, which are directly bonded to the uranyl, have a larger core-level shift than site N4/N5 situated two nearest-neighbor distances away from the uranyl. Still, a core-level shift of 0.63 eV on N4/N5 suggests that the change in electron density upon complexation is distributed over the bbp framework. Shifts observed in the NEXAFS peaks, however, are much smaller as resonant X-ray excitation energies also include the change in conduction band energies upon complexation, which would largely be in the same direction as the core-level shift owing to the common change in the underlying local potential. Moreover, hybridization effects in the core-excited final state can further modulate the excitation energy. Thus, we see that in the case of site N4, the calculated NEXAFS onset is actually red-shifted in complex **1** relative to H_2bbp even though we predict the 1s core-level binding energy is blue-shifted. In Figure 6, the wave functions of the conduction band minimum occupied by the excited core−electron for 1s excitations on different N sites are shown. It is apparent that the final state is strongly dependent on the excitation site. A core excitation on N2 from the pyridine segment of the bbp produces a final state that is also distributed in a symmetric manner over the two benzimidazole segments. On the other hand, final states for excitations on the imidazole-type sites N1, N4 are confined to the benzimidazole segment containing these sites with some weight also on the pyridine segment. Excitations on N3, N5 similarly lead to final state electronic wave functions confined to the other benzimidizaole segment. In this context we also note that we do not identify spectral signatures in the NEXAFS that can be easily attributed to N 2p−U 5f hybridization. This is because the dative interaction between bbp N and the uranyl group is characterized by weak orbital overlaps, and furthermore, as shown in Figure 4, empty U 5f states occur at higher energies relative to the lowest N 2p-derived π^* orbitals that provide the most intense N K-edge transitions near the onset. While N 2p−U 5f hybridization could contribute to some modulation of the spectral features above the onset, its contribution is not easily separated from that of other factors such as structural changes and ligand polarization that coexist.

Table 4. Calculated Core-Level Shifts ΔE_{XPS} on Specific N Sites and Corresponding Shifts in the NEXAFS Onset ΔE_{XAS} as a Result of H_2bbp Binding to Uranyl to Form Complex 1

atom	ΔE_{XPS} (eV)	ΔE_{XAS} (eV)
N2	0.98	0.26
N1	0.96	0.18
N4	0.63	−0.61

4.3.2. Effect of Pyridine Ligand Substitution. Starting from complex **1** and considering overall changes in ligand composition, we see that complexes **2** and **3** involve sequential substitution of Cl^- ions in the coordination sphere of uranyl with Py ligands and an increase in charge on the bbp ligand as a result of deprotonation of the benzimidazole group. The net result is an increase in electron density on the bbp ligand and a strengthening of the bbp−uranyl bonding as evidenced by shorter U−N bonds[17] (see section 4.1). The increased charge on the ligand is primarily distributed over the π-conjugated benzimidazole group that is deprotonated. We quantify this effect on the N sites of the bbp that are of interest, through their Lowdin[54] populations (n_{Lowdin}) as shown in Table 5. For

Table 5. Lowdin Populations (n_{Lowdin}) on Various N Sites on Complexes 1−3 and Distances (r_{WFC}) between Wannier Function Centers Located along Various Bonds and the N Donor Sites Participating in Those Bonds

	n_{Lowdin}			r_{WFC} (Å)		
atom	$UO_2(H_2bbp)Cl_2$	$UO_2(Hbbp)Py{\cdot}Cl$	$UO_2(bbp)Py_2$	$UO_2(H_2bbp)Cl_2$	$UO_2(Hbbp)Py{\cdot}Cl$	$UO_2(bbp)Py_2$
N1	5.248	5.333	5.346	0.433 (N−U)[a]	0.494 (N−U)[a]	0.496 (N−U)[a]
N2	5.198	5.222	5.235	0.425 (N−U)	0.462 (N−U)	0.492 (N−U)
N3	5.247	5.266	5.345	0.429 (N−U)	0.448 (N−U)	0.497 (N−U)
N4	5.236	5.311	5.306	0.590 (N−H)	0.359 (LP)[b]	0.351 (LP)[b]
N5	5.235	5.232	5.306	0.589 (N−H)	0.587 (N−H)	0.351 (LP)
N6		5.200	5.216		0.471 (N−U)	0.456 (N−U)
N7			5.216			0.456 (N−U)

[a]The type of bond is indicated in parentheses. [b]LP denotes a lone pair.

dx.doi.org/10.1021/ic501107a | Inorg. Chem. 2014, 53, 11415−11425

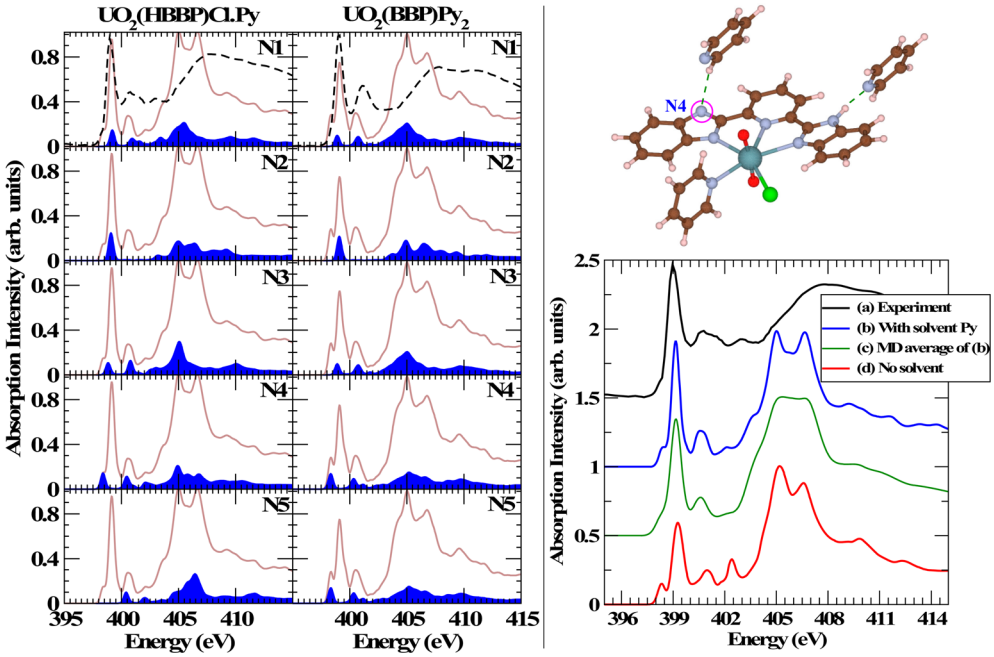

Figure 7. (left) Decomposition of the simulated N K edge NEXAFS spectra of complexes **2** and **3** into contributions from specific N sites. The blue shared region in each panel depicts the specific site contribution against the total spectrum shown in brown. The experimental spectrum is shown as a dashed line in the upper panel. (upper right) Structural model for a molecular unit of complex **2** hydrogen bonded to solvent pyridine molecules. Hydrogen bonds are indicated as dashed green lines. (lower right) Theoretical N K-edge NEXAFS spectra (b, c, d) of complex **2** from structural models with and without solvent pyridine molecules are compared to experiment (a).

instance, the sites N1 and N4 in complex **2** belonging to the deprotonated benzimidazole, exhibit roughly a 1.6% increase in the n_{Lowdin} relative to their counterparts in complex **1**. Also, site N1, which bonds to the uranium in the uranyl moiety, has a slightly higher n_{Lowdin} compared to N4, which indicates a higher degree of anionic character on the former. The same trend is continued in complex **3** in which the benzimidazole group hosting sites N3 and N5 is also deprotonated. This clearly shows that the anionic charge in the mono- (bbp^{-}) and dideprotonated (bbp^{2-}) ligands is delocalized over the entire congugated framework of the benzimidale groups and not confined just to the N4/N5 sites that are orginally proton-bonded in the neutral bbp ligand. We also note that donor sites N6 and N7 on the Py ligands replacing the Cl^{-} ligands have a similar n_{Lowdin} as that of site N2 on the deprotonated bbp^{2-} ligand. The shortening of the uranyl to bbp N-donor bond distances in going from **1** to **3** should also be reflected in a modulation of the electron density distribution in the direction of increasing covalency. This can be gauged by investigating the positions of the centers of MLWFs[52,55] introduced earlier (see section 4.3.1). The position of a Wannier function center (WFC) located along a bond between two atoms provides qualitative information regarding the degree of covalency, with the WFC shifting toward the bond-center with increasing covalency. In Table 5 we show the distances ($\mathbf{r}_{\mathrm{WFC}}$) between N atoms and WFCs situated along various N−U and N−H bonds. Comparing the situation in complex **2** to that in complex **1**, we find that WFCs along bonds connecting the donor sites N1, N2, and N3 to uranyl are farther away from the N sites in **2** than in **1**. This indicates that the average positions of the electrons involved in the bbp−uranyl bonding interaction shift slightly toward the uranyl in complex **2**. This trend is further enhanced in complex **3**. Note that in the case of sites N4 and N5 that are sequentially deprotonated, the WFC shifts significantly closer to the N upon deprotonation and nominally indicates a lone-pair configuration (denoted LP in Table 5). Using the same metric, we also conclude that in complex **3**, the bonding between uranyl and the Py ligands is slightly weaker than the uranyl−bbp interaction.

Changes in the electronic structure described above lead to subtle modulations in the NEXAFS spectra from complexes **2** and **3**. A deconvolution of the theoretical NEXAFS spectra of complexes **2** and **3** into contributions from different N sites on the bbp ligand is shown in Figure 7. As in the case of complex **1**, we find that in both **2** and **3** feature A at ∼399 eV (see Figure 5) originates from the first 1s → π^* excitations on N1, N2, and N3. Feature B in complex **2** is attributed to contributions from the second 1s → π^* excitation on N1, N3, and N4 as well as the first 1s → π^* on N5, while peak D is attributed to the second and third sets of 1s → π^* transitions on N5 and N4, respectively. In complex **3** peak B is the only other prominent feature observed close to the absorption edge in addition to peak A, and it is seen to have contributions from the second 1s → π^* transition on N1, N3, N4, and N5. Peak D is notably absent in complex **3**, and this is attributed to the lack of protonated N4/N5 sites. We see from Figure 7 that both N4 and N5, which are deprotonated in **3**, have their second 1s → π^* occurring at a lower energy compared to when protonated and, hence, have no significant absorption near 402.8 eV. Notice that a feature D′ (see Figure 5) is observed in the corresponding precursor Na_2bbp as one of the sites (N4 in Figure 2) is bonded to Na and has its spectrum blue-shifted relative to the fully deprotonated case. We note that in complexes **2** and **3**, the additional N sites N6/N7 from pyridine ligands have a similar spectral contribution to that of N2 in the near-edge region. Thus, they mainly contribute toward enhancing feature A.

dx.doi.org/10.1021/ic501107a | *Inorg. Chem.* 2014, 53, 11415−11425

In Figure 8, we focus on the three binding sites N1−N3 of bbp and follow the variation in the K-edge absorption of each

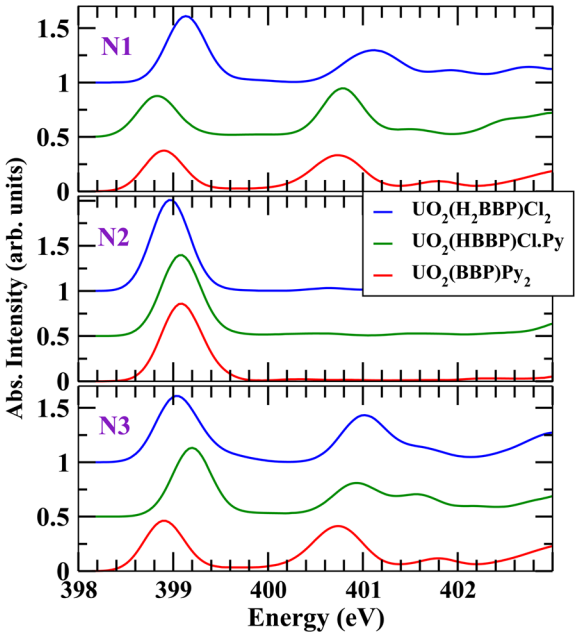

Figure 8. Evolution of the K-edge absorption onset of each of the three metal-binding sites N1−N3 as a function of the changing ligand character around the uranyl core, going from complex **1** to **3**.

individual site as a function of the changing uranyl coordination going from complex **1** to **3**. The pyridine site N2 does not show much variability except for a small blue shift of about 80 meV in complexes **2** and **3** relative to that of complex **1**. This shift is attributed to an interplay between the shortening of the U−N1 bond length (from 2.63 Å in **1** to 2.53 Å in **3**), which tends to blue-shift the spectrum and increase electron density on the bbp ligand in **2** and **3**, which has the opposite effect. Interestingly, the spectra of N1 and N3 in complex **2** show relative shifts with respect to **1** of opposite sign, which reflects the strong asymmetry about the uranyl in **2** because of dissimilar ligands. N1, which is on the deprotonated benzimidazole and closer to the Py ligand, shows a red shift, while N3, which is on the protonated benzimidazole and closer to Cl^-, shows a blue shift. In complex **3**, the spectra of both N1 and N3 are red-shifted relative to **1**, as the uranyl coordination is once again symmetric, and both sites feel the effect of the increased change on the dideprotonated bbp^{2-} ligand.

4.3.3. Deprotonation and Solvent Interaction Effects. The effect on the spectrum of the successive deprotonation of sites N4 and N5 in **2** and **3** is also worth discussing. We see from Figure 7 that the deprotonated N4 site in complex **2** has a significantly lower absorption onset than protonated site N5. In fact, the first 1s → π^* transition on N4 is lower by 2.3 eV than it is on N5. This results from the fact that the LUMO energy for this deprotonated moiety is expected to be lower by frontier orbital theory. Additionally, the deprotonated N4 has slightly higher on-site charge density than site N5, which is covalently bonded to H (see Table 5). In turn this leads to a lower binding energy for the 1s core electron on N4 relative to N5. These effects cooperate resulting in a smaller 1s → π^* excitation energy on N4. In our calculations for complex **2**, the first 1s → π^* transition on N4 occurs at 398.4 eV, which is ∼0.6 eV below peak A and therefore appears as a small additional shoulder near the absorption onset. This feature is barely apparent in experiment (see Figure 7) because of thermal broadening[56,57] at room temperature. To ascertain that this is indeed the case, we recalculated the spectrum of complex **2**, explicitly taking into account broadening from ionic dynamics at 300 K. This was conducted by first obtaining a first-principles Born−Oppenheimer molecular dynamics (MD) trajectory of the molecular crystal of complex **2** at 300 K, calculating the N K-edge spectra at 20 individual points separated by 100 fs along the trajectory and subsequently averaging over all such spectra. This led to a spectrum with a slightly broader feature A, with the pre-edge no longer apparent as a separate peak but only as an inflection in the line shape similar to the one seen in experiment. Recall, however, that in the molecular crystal of complex **2**, additional Py solvent molecules are hydrogen bonded to the outer N4 and N5 sites. The structural model for one such molecular unit from a crystal is shown in Figure 7. Interestingly, we find that in the absence of solvent Py molecules the pre-edge shoulder appears more prominently as a distinct peak at 398.3 eV. Additionally, in the unsolvated case, the energy position of peak A is also shifted slightly higher to 399.3 eV from its position at 399.1 eV in the solvated case. This further enhances the appearance of the pre-edge feature as a distinct peak. The lack of additional Py solvent molecules also means the contribution from excitations on the deprotonated N4 site is proportionately larger in the overall NEXAFS specturm.

In complex **3**, which has two deprotonated imidazole sites, 1s → π^* transitions on N4 and N5 are predicted to lead to a similar pre-edge feature at 398.3 eV, ∼0.8 eV below peak A at 399.1 eV. The feature is somewhat more prominent than in complex **2** because there are twice as many deprotonated N sites, and it therefore appears as a distinct pre-edge peak (labeled **e** in Figure 5). However, the peak is not observed in the experimental spectrum, and we attribute this to the possible presence of additional free Py hydrogen-bonded to the N4 and N5 sites in the experimental samples. Indeed while solvent molecules were not identified by XRD studies on the molecular crystal of complex **3**, NMR studies on the samples used for NEXAFS measurements did indicate the presence of free Py (see Supporting Information). We speculate that if uranyl−bbp complexes can be synthesized in solvents that do not contain nitrogen and ideally do not form hydrogen bonds easily, it would be possible to detect the excitations on the deprotonated imidazole sites as a pre-edge feature in the NEXAFS spectrum.

Finally we remark on the lack of pre-edge-like features in the experimental and theoretical spectra of precursors NaHbbp and Na_2bbp even though they host deprotonated imidazole sites N4/N5 (see Figure 2). Our analysis shows that while the first 1s → π^* transitions on the deprotonated N4/N5 sites in the precursors also occur at a lower energy than the corresponding excitations on sites N1−N3 that lead to peak A, the two sets of excitations are closer in energy and thus do not appear as distinct peaks. For instance in Na_2bbp, the lowest energy 1s → π^* transition on N5 occurs at 398.4 eV but is only 0.5 eV separated from peak A at 398.9 eV and therefore is not apparent as a separate pre-edge within characteristic thermal broadening.[56,57]

5. CONCLUSIONS

We have investigated the electronic structure of three N-donor uranyl complexes $[UO_2(H_2bbp)Cl_2]$ (**1**), $[UO_2(Hbbp)(Py)Cl]$ (**2**), and $[UO_2(bbp)(Py)_2]$ (**3**) by combining experimental N

dx.doi.org/10.1021/ic501107a | *Inorg. Chem.* 2014, 53, 11415−11425

K-edge NEXAFS measurements with first-principles DFT calculations and NEXAFS simulations. Complexes **1**−**3** contain derivatives of the versatile N-donor ligand 2,6-bis(2-benzimidazyl)pyridine (bbp) and additional Cl^- and pyridine ligands in the equatorial uranyl plane. A combination of steric and electronic effects leads to a systematic evolution of the structural and electronic properties of these complexes.

Ground-state DFT calculations show that the largely π-conjugated framework of bbp is significantly polarized in bonding to uranyl. Furthermore, Py solvent molecules incorporated into molecular crystals of complex **2** are seen to affect the uranyl−bbp binding geometry suggesting that the dative bonding between $\{UO_2\}^{2+}$ and the N donor sites of bbp is sensitive to weak interactions in the environment of the bbp ligand such as hydrogen bonding to solvent molecules. A decrease in U═O hybridization in the $\{O{=}U{=}O\}^{2+}$ moiety is observed within complexes **2** and **3** relative to **1** as the coordination environment about uranyl is modified and charge on the bbp ligand increased. This goes together with increasing on-site Coulomb repulsion on the uranium site as evidenced by the larger self-consistent *U* parameter for complexes **2** and **3** in our DFT+*U* calculations. In contrast, increased charge on the bbp ligand combined with reduced steric hindrance leads to shorter bbp−uranyl bonds in complexes **2** and **3**, which are indicated as more covalent by Wannier center displacement analysis.

NEXAFS spectra of the complexes show a systematic blue shift of ∼0.2 eV with respect to those of the corresponding precursors. This arises from the deepening of N 1s core levels in the complexes driven by charge displacement toward the uranyl upon complexation. The blue shift, which we expect to be common to polarizable ligand systems, is particularly apparent in the lowest 1s → π^* transition on the central pyridine-like N site of bbp. Changes in ligand character in the outer coordination shell of the uranyl lead to subtle differences in the spectral features of N sites on bbp. These can be interpreted with the help of theoretical simulations that facilitate decomposition of the compound NEXAFS spectrum into individual atomic site contributions. Successive deprotonation of the outer imidazole sites of bbp in complexes **2** and **3**, which occurs in conjunction with Cl^- groups being replaced by Py groups around the uranyl, results in a significant modulation of the spectra. Increased electron density on the benzimidazole groups of the mono- and di-deprotonated bbp^- and bbp^{2-} ligands leads to reduced N 1s core-level binding and significantly lower 1s → π^* transition energies relative to the protonated bbp ligand. This in turn gives rise to pre-edge features at the absorption onset, which, interestingly, are modulated by solvent molecules incorporated into the molecular crystals. Finally we comment on the sensitivity of K-edge NEXAFS as a probe of electronic structure in N-donor uranyl complexes. We find that N K-edge NEXAFS is highly sensitive to changes associated with new bond formation or bond breaking as well as charge-density polarization of the π-conjugated framework. However, small changes in the inherently weak N-uranyl dative interaction are difficult to track using this method, as signatures of N 2p−U 5f hybridization are not readily apparent in the spectral features. Alternative metrics such as displacements in Wannier function centers, available from first-principles calculations, are therefore necessary to provide complementary information toward better understanding N-uranyl bonding in these complexes.

■ ASSOCIATED CONTENT

Ⓢ Supporting Information

NMR spectral analysis of complexes **2** and **3**, NEXAFS data from STXM measurements. This material is available free of charge via the Internet at http://pubs.acs.org.

■ AUTHOR INFORMATION

Corresponding Author

*E-mail: scpemmaraju@lbl.gov.

Present Addresses

⊗(R.C.) Inorganic, Isotope and Actinide Chemistry Group, Los Alamos National Laboratory, Los Alamos, NM 87545 USA.

○(S.W.) School of Radiation Medicine and Protection (SRMP) and School of Radiological and Interdisciplinary Sciences (RAD-X), Soochow University, Suzhou, Jiangsu 215123, China.

Notes

The authors declare no competing financial interest.

■ ACKNOWLEDGMENTS

Theoretical and computational work by C.D.P. and D.P. was supported by the Laboratory Directed Research and Development Program of Lawrence Berkeley National Laboratory (LBNL) and as a User Project at the Molecular Foundry, LBNL. D.K.S, R.C., and S.W. were also supported by the Laboratory Directed Research and Development Program at LBNL. Calculations were performed on Hopper, at the National Energy Research Scientific Computing Center, LBNL and Molecular Foundry computing resources, Nano and Vulcan, managed by the High Performance Computing Services Group, LBNL. All LBNL work is supported by the Office of Science of the U.S. Department of Energy under Contract No. DE-AC02-05CH11231. The Advanced Light Source is supported by the Director, Office of Science, Office of Basic Energy Sciences; and the MES Beamline by the aforementioned office, Division of Chemical Sciences, Geosciences, and Biosciences; both of the U.S. Department of Energy under Contract No. DE-AC02-05CH11231 at LBNL.

■ REFERENCES

(1) Ephritikhine, M. *Dalton Trans.* **2006**, 2501−2516.

(2) Burns, C.; Eisen, M. Organoactinide Chemistry: Synthesis and Characterization. In *The Chemistry of the Actinide and Transactinide Elements SE - 25;* Morss, L.; Edelstein, N.; Fuger, J., Eds.; Springer: Netherlands, 2006; pp 2799−2910.

(3) Fortier, S.; Hayton, T. W. *Coord. Chem. Rev.* **2010**, *254*, 197−214.

(4) Jones, M. B.; Gaunt, A. J. *Chem. Rev.* **2013**, *113*, 1137−1198.

(5) Hayton, T. W. *Chem. Commun. (Cambridge, U.K.)* **2013**, *49*, 2956−2973.

(6) Lewis, F. W.; Harwood, L. M.; Hudson, M. J.; Drew, M. G. B.; Sypula, M.; Modolo, G.; Whittaker, D.; Sharrad, C. A.; Videva, V.; Hubscher-Bruder, V.; et al. *Dalton Trans.* **2012**, *41*, 9209−9219.

(7) Lewis, F. W.; Harwood, L. M.; Hudson, M. J.; Drew, M. G. B.; Desreux, J. F.; Vidick, G.; Bouslimani, N.; Modolo, G.; Wilden, A.; Sypula, M.; et al. *J. Am. Chem. Soc.* **2011**, *133*, 13093−13102.

(8) Maynadié, J.; Berthet, J.-C.; Thuéry, P.; Ephritikhine, M. *Chem. Commun. (Cambridge, U.K.)* **2007**, 486−488.

(9) Tatsumi, K.; Hoffmann, R. *Inorg. Chem.* **1980**, *19*, 2656−2658.

(10) Denning, R. G. Electronic Structure and Bonding in Actinyl Ions. In *Complexes, Clusters and Crystal Chemistry SE - 4;* Structure and Bonding; Springer: Berlin, Heidelberg, 1992; Vol. *79*, pp 215−276.

(11) Denning, R. G.; Green, J. C.; Hutchings, T. E.; Dallera, C.; Tagliaferri, A.; Giarda, K.; Brookes, N. B.; Braicovich, L. *J. Chem. Phys.* **2002**, *117*, 8008.

(12) Denning, R. G. *J. Phys. Chem. A* **2007**, *111*, 4125−4143.

(13) Spencer, L. P.; Yang, P.; Minasian, S. G.; Jilek, R. E.; Batista, E. R.; Boland, K. S.; Boncella, J. M.; Conradson, S. D.; Clark, D. L.; Hayton, T. W.; et al. *J. Am. Chem. Soc.* **2013**, *135*, 2279−2290.
(14) Kozimor, S. A.; Yang, P.; Batista, E. R.; Boland, K. S.; Burns, C. J.; Clark, D. L.; Conradson, S. D.; Martin, R. L.; Wilkerson, M. P.; Wolfsberg, L. E. *J. Am. Chem. Soc.* **2009**, *131*, 12125−12136.
(15) Fillaux, C.; Guillaumont, D.; Berthet, J.-C.; Copping, R.; Shuh, D. K.; Tyliszczak, T.; Den Auwer, C. *Phys. Chem. Chem. Phys.* **2010**, *12*, 14253−14262.
(16) Sonnenberg, J. L.; Hay, P. J.; Martin, R. L.; Bursten, B. E. *Inorg. Chem.* **2005**, *44*, 2255−2262.
(17) Copping, R.; Jeon, B.; Das Pemmaraju, C.; Wang, S.; Teat, S. J.; Janousch, M.; Tyliszczak, T.; Canning, A.; Grønbech-Jensen, N.; Prendergast, D.; et al. *Inorg. Chem.* **2014**, *53*, 2506−2515.
(18) Drew, M. G. B.; Hill, C.; Hudson, M. J.; Iveson, P. B.; Madic, C.; Vaillant, L.; Youngs, T. G. A. *New J. Chem.* **2004**, *28*, 462.
(19) Escande, A.; Guénée, L.; Buchwalder, K.-L.; Piguet, C. *Inorg. Chem.* **2009**, *48*, 1132−1147.
(20) Muller, G.; Bünzli, J.-C. G.; Schenk, K. J.; Piguet, C.; Hopfgartner, G. *Inorg. Chem.* **2001**, *40*, 2642−2651.
(21) Petoud, S.; Bünzli, J.-C. G.; Schenk, K. J.; Piguet, C. *Inorg. Chem.* **1997**, *36*, 1345−1353.
(22) Petoud, S.; Bünzli, J.-C. G.; Glanzman, T.; Piguet, C.; Xiang, Q.; Thummel, R. P. *J. Lumin.* **1999**, *82*, 69−79.
(23) Piguet, C.; Buenzli, J. C. G.; Bernardinelli, G.; Hopfgartner, G.; Williams, A. F. *J. Am. Chem. Soc.* **1993**, *115*, 8197−8206.
(24) Stöhr, J. *NEXAFS Spectroscopy;* Springer Series in Surface Sciences; Springer: Berlin, Heidelberg, 1992; Vol. 25, p 6221.
(25) Groot, F. de; Kotani, A. *Core Level Spectroscopy of Solids;* CRC Press 2008;.
(26) Tanaka, I.; Mizoguchi, T. *J. Phys.: Condens. Matter* **2009**, *21*, 104201.
(27) Shuh, D.; Copping, R.; Tyliszczak, T.; Castro-Rodriguez, I.; Shuh, D. K. *Mater. Res. Soc. Symp. Proc.* **2008**, *1104*, 1104−NN06−06.
(28) Rehr, J. J. *Rev. Mod. Phys.* **2000**, *72*, 621−654.
(29) Shirley, E. *Phys. Rev. Lett.* **1998**, *80*, 794−797.
(30) Olovsson, W.; Tanaka, I.; Puschnig, P.; Ambrosch-Draxl, C. *J. Phys.: Condens. Matter* **2009**, *21*, 104205.
(31) Prendergast, D.; Galli, G. *Phys. Rev. Lett.* **2006**, *96*, 215502.
(32) Solomon, E. I.; Hedman, B.; Hodgson, K. O.; Dey, A.; Szilagyi, R. K. *Coord. Chem. Rev.* **2005**, *249*, 97−129.
(33) Prüßmann, T.; Denecke, M. A.; Geist, A.; Rothe, J.; Lindqvist-Reis, P.; Löble, M.; Breher, F.; Batchelor, D. R.; Apostolidis, C.; Walter, O.; et al. *J. Phys. Conf. Ser.* **2013**, *430*, 012115.
(34) Roos, B. O.; Malmqvist, P.-A.; Gagliardi, L. *J. Am. Chem. Soc.* **2006**, *128*, 17000−17006.
(35) Gagliardi, L.; Roos, B. O. *Chem. Soc. Rev.* **2007**, *36*, 893−903.
(36) Hohenberg, P. *Phys. Rev.* **1964**, *136*, B864−B871.
(37) Kohn, W.; Sham, L. J. *Phys. Rev.* **1965**, *140*, A1133−A1138.
(38) Mahan, G. *Many Particle Physics,* 3rd ed.; Kluwer Academic/Plenum: New York, NY, 2000.
(39) England, A. H.; Duffin, A. M.; Schwartz, C. P.; Uejio, J. S.; Prendergast, D.; Saykally, R. J. *Chem. Phys. Lett.* **2011**, *514*, 187−195.
(40) Jiang, P.; Prendergast, D.; Borondics, F.; Porsgaard, S.; Giovanetti, L.; Pach, E.; Newberg, J.; Bluhm, H.; Besenbacher, F.; Salmeron, M. *J. Chem. Phys.* **2013**, *138*, 024704.
(41) Anisimov, V. I.; Aryasetiawan, F.; Lichtenstein, A. I. *J. Phys.: Condens. Matter* **1997**, *9*, 767−808.
(42) Cococcioni, M.; de Gironcoli, S. *Phys. Rev. B* **2005**, *71*, 035105.
(43) Kulik, H. J.; Cococcioni, M.; Scherlis, D. A.; Marzari, N. *Phys. Rev. Lett.* **2006**, *97*, 103001.
(44) Kresse, G. *Phys. Rev. B* **1996**, *54*, 11169−11186.
(45) Giannozzi, P.; Baroni, S.; Bonini, N.; Calandra, M.; Car, R.; Cavazzoni, C.; Ceresoli, D.; Chiarotti, G. L.; Cococcioni, M.; Dabo, I.; et al. *J. Phys.: Condens. Matter* **2009**, *21*, 395502.
(46) Perdew, J. P.; Burke, K.; Ernzerhof, M. *Phys. Rev. Lett.* **1996**, *77*, 3865−3868.
(47) Blöchl, P. E. *Phys. Rev. B* **1994**, *50*, 17953−17979.
(48) Prendergast, D.; Louie, S. G. *Phys. Rev. B* **2009**, *80*, 235126.
(49) Momma, K.; Izumi, F. *J. Appl. Crystallogr.* **2011**, *44*, 1272−1276.
(50) Perdew, J. P. *Phys. Rev. B* **1981**, *23*, 5048−5079.
(51) Chen, W.; Wu, X.; Car, R. *Phys. Rev. Lett.* **2010**, *105*, 017802.
(52) Marzari, N.; Vanderbilt, D. *Phys. Rev. B* **1997**, *56*, 12847−12865.
(53) Boys, S. F. In *Quantum Theory of Atoms;* Lowdin, P. O., ed.; Academic: New York, 1966.
(54) Löwdin, P.-O. *J. Chem. Phys.* **1950**, *18*, 365.
(55) Marzari, N.; Souza, I.; Vanderbilt, D. *Psi-K Newsl.* **2003**, 129−168.
(56) Uejio, J. S.; Schwartz, C. P.; Saykally, R. J.; Prendergast, D. *Chem. Phys. Lett.* **2008**, *467*, 195−199.
(57) Pascal, T. A.; Boesenberg, U.; Kostecki, R.; Richardson, T. J.; Weng, T.-C.; Sokaras, D.; Nordlund, D.; McDermott, E.; Moewes, A.; Cabana, J.; et al. *J. Chem. Phys.* **2014**, *140*, 034107.